Journal of The Electrochemical Society

The Electrochemical Society
Advancing solid state & electrochemical science & technology

OPEN ACCESS

# Modeling the Impact of Manufacturing Uncertainties on Lithium-Ion Batteries

To cite this article: Oke Schmidt *et al* 2020 *J. Electrochem. Soc.* **167** 060501

View the article online for updates and enhancements.


This content was downloaded from IP address 134.169.218.80 on 25/05/2020 at 07:59

*Journal of The Electrochemical Society*, 2020 **167** 060501

# Modeling the Impact of Manufacturing Uncertainties on Lithium-Ion Batteries

**Oke Schmidt,[1,2] Matthias Thomitzek,[2,3] Fridolin Röder,[1,2] Sebastian Thiede,[2,3] Christoph Herrmann,[2,3] and Ulrike Krewer[1,2,z]**

[1]*Institute of Energy and Process Systems Engineering, TU Braunschweig, Braunschweig, Germany*
[2]*Battery LabFactory Braunschweig (BLB), TU Braunschweig, Braunschweig, Germany*
[3]*Institute of Machine Tools and Production Technology, TU Braunschweig, Braunschweig, Germany*

This paper describes and analyzes the propagation of uncertainties from the lithium-ion battery electrode manufacturing process to the structural electrode parameters and the resulting varying electrochemical performance. It uses a multi-level model approach, consisting of a process chain simulation and a battery cell simulation. The approach enables to analyze the influence of tolerances in the manufacturing process on the process parameters and to study the process-structure-property relationship. The impact of uncertainties and their propagation and effect is illustrated by a case study with four plausible manufacturing scenarios. The results of the case study reveal that uncertainties in the coating process lead to high deviations in the thickness and mass loading from nominal values. In contrast, uncertainties in the calendering process lead to broad distributions of porosity. Deviations of the thickness and mass loading have the highest impact on the performance. The energy density is less sensitive against porosity and tortuosity as the performance is limited by theoretical capacity. The latter is impacted only by mass loading. Furthermore, it is shown that the shape of the distribution of the electrochemical performance due to parameter variation aids to identify, whether the mean manufacturing parameters are close to an overall performance optimum.
© 2020 The Author(s). Published on behalf of The Electrochemical Society by IOP Publishing Limited. This is an open access article distributed under the terms of the Creative Commons Attribution 4.0 License (CC BY, http://creativecommons.org/licenses/by/4.0/), which permits unrestricted reuse of the work in any medium, provided the original work is properly cited. [DOI: 10.1149/1945-7111/ab798a]

Manuscript submitted November 22, 2019; revised manuscript received January 21, 2020. Published March 18, 2020.

Today's environmental challenges like global warming and air pollution demand to improve the energy and mobility technologies toward sustainability. Electric vehicles, i.e. $CO_2$ free mobility (depending on the applied electricity generation) and the use of renewable energy sources are crucial for reaching the goal of limiting global warming. In terms of mobility, the lithium-ion battery is one of the most promising technologies to take the first steps toward electrification. To present an attractive alternative to the classical combustion technology, the lithium-ion battery needs to be efficient, safe and affordable.

The performance of a lithium-ion battery is described by its electrochemical performance properties, such as energy density, power density and capacity. These properties strongly depend on the electrode structure generated in the manufacturing process, which consists of a number of individual steps.[1] Due to machine tolerances, deviations can occur at every manufacturing step. This creates uncertainties in the structural parameters of the intermediate and the final product. The intensity of the deviations has an effect on pack durability and on the rejection rate, i.e. the percentage of produced but discarded batteries.[2] Due to the high material costs of the batteries, the rejection rate is also crucial in order to further reduce battery costs and thus enhance market acceptance, e.g. for electric vehicles.[3] For optimizing the quality of the manufactured lithium-ion batteries and reducing the costs, it is necessary to understand how these uncertainties emerge and how they affect the structural parameters and the electrochemical performance properties of the battery.

These uncertain structural parameters lead to deviations of the electrochemical properties, which cause variations on cell level and affect the lifetime and overall performance. An et al.[4] presented an experimental based analysis of cell-to-cell variations. The rate dependence of these variations was studied with a statistically relevant amount of commercial cells, focusing on the correlation of capacity vs weight and capacity vs resistance and the kinetics. For small rates of 0.2 C, a nearly linear correlation with the cell weight was identified. Increasing the rate leads to a more non-linear behavior due to the increased effect of the kinetics. Experimental work that investigates process uncertainties is rare, since it requires significant amount of manufactured cells and high number of electrochemical measurements.

The costs and time required can be reduced by selecting suitable electrochemical models to analyze the effect of uncertain structural parameters on the electrochemical performance. In the work of Santhanagopalan et al.[5] the influence of cell-to-cell variations on the impedance was analyzed. The effect of the structural parameters of different components on the cell impedance was analyzed and the sensitive parameters and components were identified. Nan et al.[6] conducted a polynomial chaos expansion (PCE) based sensitivity analysis with a 3D multiphysics model of a multilayer cell. It was concluded that the cell discharge capacity and the thermal behavior at 1 C are most sensitive to the electrode parameters and their pore structure. In the work of Hadigol et al.[7] the effect of parametric model uncertainties on the cell capacity, voltage and concentrations was studied. The focus was set on a limited number of structural parameters, e.g. porosity, particle size and bruggeman coefficient, and a greater number of kinetic parameters. Additionally to the presented literature, Laue et al.[8] studied the influence of cell-to-cell variations and subcell variations. It was concluded that subcell deviations, i.e. deviations within a single electrode sheet, have a significant impact on the overall cell behavior. However, the influence of the manufacturing processes on the examined structures was not taken into account in these presented model based approaches. This impedes a consecutive consideration of the propagation of uncertainties from the machine defined process parameters to the evolving structural parameters and to the electrochemical properties.

The continuous description of deviations in the manufacturing processes and their influence on the electrochemical properties requires to couple the model based approaches from the field of process engineering with that of the electrochemical systems engineering. Ngandjong et al.[9] applied a multiscale simulation platform to understand the formation of various electrode structures and to enable a detailed prediction of the electrochemical performance. Further, Chouchane et al.[10] used the platform to investigate the impact of carbon-binder spatial location on the electrochemical performance properties and Rucci et al.[11] used it to track the variabilities arising on the simulation level.

In contrast, this work focuses on process induced uncertainties and its propagation throughout the process chain to enable

[z]E-mail: u.krewer@tu-braunschweig.de

identification of the most relevant process parameters to lower manufacturing discard. This requires a computationally efficient framework. Therefore, we apply a homogenized cell model in combination with analytical models for single process steps. Homogenized cell models are frequently applied to study the impact of structural parameters on cell performance, which has been used for example by Lenze et al.[12] to investigate the impact of the calendering process, by Smekens et al.[13] to analyze the impact of the electrode density on the performance and by Kenney et al.[14] to study the impact of variations in the structural parameters. Analytical process models are commonly developed in process engineering as for example by Mayer et al.[15] for the mixing and dispersing process and by Jaiser et al.[16] for the drying process. Process chain simulations enable to cover process interactions by coupling single process models as has been shown by Schönemann et al.[17] In this work we couple a process chain simulation and a homogenized cell model as introduced previously by Thomitzek et al.[18] This allows a description of the electrochemical performance properties as a function of the process parameters. The approach is then used to conduct a case study with different uncertainty scenarios. The resulting variation in structural parameters is evaluated in depth by their physical impact on the electrochemical properties. This procedure identifies the most sensitive process parameters in relation to the electrochemical properties and reveals the impact of uncertainties in the manufacturing process on the product properties. This allows to identify weak points in the manufacturing process, which is needed for an knowledge-based optimization.

## Methodology

In the first part of this section, the superordinate multi-level model approach is briefly introduced. Then, for the process chain simulation, the single process models are described and in the last part the battery model for evaluating the electrochemical properties is explained.

***Multi-level model approach.—***A multi-level model approach is implemented, which was established and published priorly by the authors of this study.[18] It is designed to describe the consecutive development of structural parameters based on the applied process parameters in the manufacturing processes and rate the impact of the final product structure on the electrochemical performance properties. First, a process chain simulation determines the effect of process parameters on the structural parameters of the (intermediate) product. Then, using the determined structural parameters, a battery cell simulation generates the electrochemical performance properties. A schematic representation of the model approach is shown in Fig. 1.

By coupling the two simulation parts, the multi-level model approach is able to quantify the impact of process parameters on the electrode structure and the battery properties. Furthermore, the coupled model approach is able to identify the impact of deviations of the process parameters on the electrochemical performance properties by a holistic consideration of the uncertainty propagation from the manufacturing process up to the final product properties along the different levels of parameters, i.e. from process to structure to property. This procedure allows one to define target values for the tolerances of the process parameters. Therefore, this approach allows to generate an improved understanding of the process-structure-property relationships in battery manufacturing. In this work the process chain simulation consists of three manufacturing steps for the coating, drying and calendering, due to existing process models in the literature and the applicability of the applied battery model.

The process chain simulation is implemented in AnyLogic and the resulting structural parameters are transferred to the battery model, which is implemented in MATLAB.

***Process chain simulation.—***The process chain simulation digitally describes the production process of lithium-ion battery electrodes. Initially, raw material enters the production process and is further processed to intermediate products and eventually the final battery cell. During the production process, process parameters can alter existing structural parameters (e.g. coating thickness reduction in calendering due to line load) or create new ones (e.g. viscosity in mixing due to mixing velocity). Different process models are used to describe these cause-effect relations between process parameters and structural parameters. The process models typically consider process parameters and structural parameters of the incoming intermediate product as input variables and determine structural parameters of the outgoing (intermediate) product as output variables. Process models are combined along the process chain and thus connect the intermediate products to an integrated product flow. The resulting process chain simulation represents a platform where different process models can be included dynamically (for further information see Ref. 18). Although both physical and data-based models can be used in the process chain simulation, physical models give insights into the causes and hence enable a better process understanding. Physical models may comprise algebraic equations or more complex models such as computational fluid dynamics or discrete element method models. However, the results of highly complex models need to be transformed into short-cut models or lookup tables in order to avoid excessive computing times. All process models must be able to represent varying process and structural parameters. By combining process models, changes in structural parameters and especially the impact of their variation can be analyzed over several process steps in order to identify significant influencing process parameters.

Battery production consists of electrode production, cell production and cell conditioning.[1] The presented simulation focuses on the electrode production since the essential cell properties (e.g. mass of active material) are already determined at this step. During electrode production, the active material, binder, conductive additives and solvent are first mixed to a suspension. In a combined coating-drying process, the suspension is coated on a current collector and dried immediately thereafter. Before entering the cell production, the electrode is compressed in a calendering process and further slitted to smaller coils. The process chain simulation covers the coating, drying and calendering process. Since the three processes are successive, a propagation of uncertainties along the process chain can be determined. The models focus on the structural parameters coating thickness, coating density, porosity and tortuosity. Analytical models are applied to describe the single process steps. The models take into account the influence of a single process parameter on changes in the structure of the intermediate product. Although reality is much more complex, they are sufficient as a first approximation to describe the cause-effect relations. Process models could be refined in the future to describe detailed physics of the process, however this was out of scope for this work. The process models were applied and parametrized to a reference production line and parameter deviations from literature were used. All model results were validated individually.

*Coating model.*—The coating process defines slurry mass loading of the electrodes, e.g. via a blade gap operated process. The process model assumes a direct transfer of the height between the doctor blade gap and the current collector to the coating thickness. Based on the slurry composition the initial wet coating thickness $h_0$ can be determined (Eq. 1). Further, the solid mass loading $M_{\text{solid}}$ can be deduced (Eq. 2).

$$h_0 = \frac{\rho_{\text{Slurry}}}{M_{\text{wet}}} \quad [1]$$

$$M_{\text{solid}} = M_{\text{wet}} - M_{\text{solvent}} = \frac{M_{\text{wet}}}{1 + X_{\text{solvent},0}} \quad [2]$$

$\rho_{\text{Slurry}}$, $M_{\text{wet}}$, $M_{\text{solid}}$, $M_{\text{solvent}}$ and $X_{\text{solvent},0}$ are structural parameters of the electrode. They represent the density of the slurry after coating,

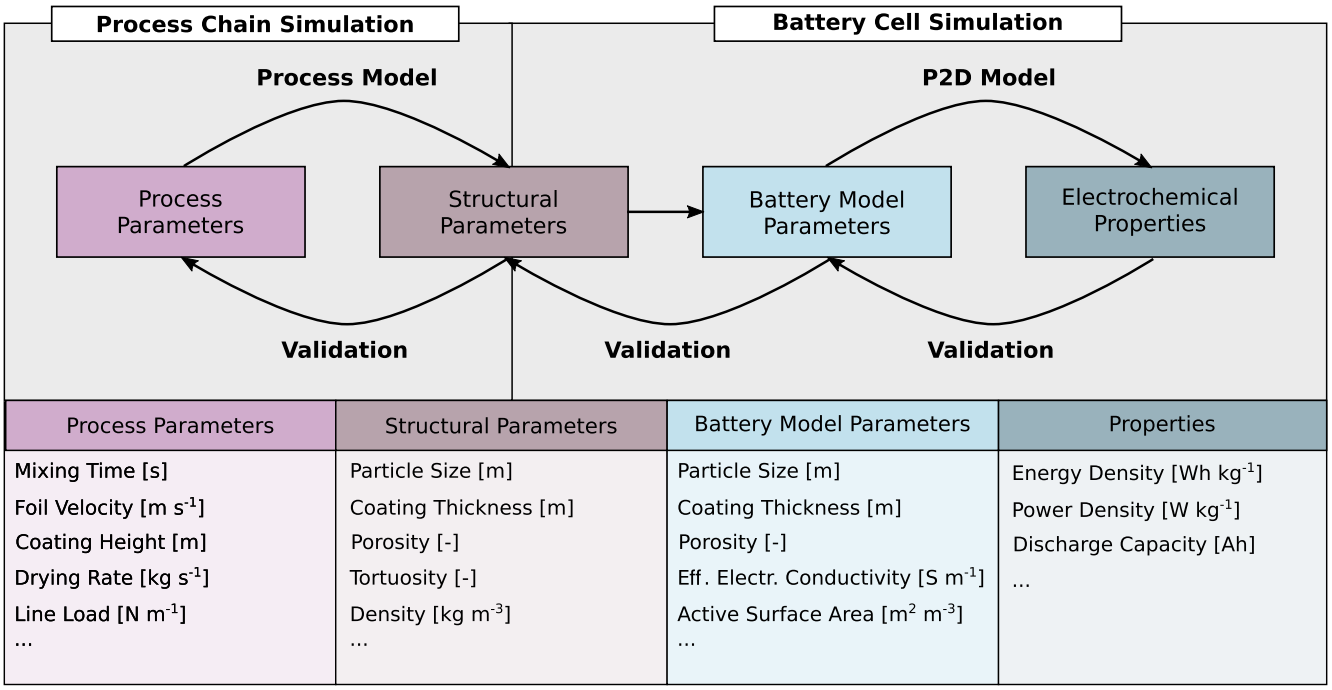


**Figure 1.** Coupled multi-level model approach, combining the process chain simulation and the battery cell simulation. For analysis of process structure property relationships. The model parameters are model input and output and thus act as interface between the single models.[18]

the mass loading of the wet film after coating, the mass loading of solids and the solvent, and the liquid-to-solid ratio of the coating. $h_0$ is the process parameter during the coating which sets the initial wet coating thickness.

*Drying model.*—In the drying process, the solvent is removed from the coated electrode. The drying process was modeled according to Jaiser et al.[16] There, the authors assume a linear relation between drying time $t$ and the decrease in coating thickness until the end of film shrinkage due to the constant drying rate $\dot{m}$. Equation 3 determines the time until the end of film shrinkage is reached. The decreasing coating thickness was modeled using Eq. 4. The solvent of the slurry evaporates steadily causing a decrease in film thickness. As the coating consolidates, pores start to empty. The coating thickness of the electrode after drying is modeled by Eq. 5.[19] The coating density initially increases until the end of film shrinkage is reached due to the decrease in coating volume but eventually decreases due to further solvent evaporation and the development of the porous structure. The coating density of the dry film can be determined by Eq. 6.

$$t_{\mathrm{EoFS}} = \frac{X_{\mathrm{solvent},0} - X_{\mathrm{solvent,EoFS}}}{\dot{m}} \cdot M_{\mathrm{solid}} \quad [3]$$

$$h(t) = h_0 - \frac{h_0 - h_{\mathrm{dry}}}{t_{\mathrm{EoFS}}} \cdot t \quad [4]$$

$$h_{\mathrm{dry}} = \frac{M_{\mathrm{solid}}}{\rho_{\mathrm{PM}} \cdot (1 - \varepsilon_{\mathrm{dry}})} \quad [5]$$

$$\rho_{\mathrm{dry}} = \frac{M_{\mathrm{solid}}}{h_{\mathrm{dry}}} \quad [6]$$

$t_{\mathrm{EoFS}}$, $t$ and $\dot{m}$ are process parameters. The parameters represent the time until the end of film shrinkage, the overall drying time and the drying rate. $X_{\mathrm{solvent},0}$, $X_{\mathrm{solvent,EoFS}}$, $h(t)$, $h_{\mathrm{dry}}$, $\rho_{\mathrm{PM}}$, $\rho_{\mathrm{dry}}$ and $\varepsilon_{\mathrm{dry}}$ are structural parameters of the coating describing the initial liquid-to-solid ratio after coating, the liquid-to-solid ratio at end of film shrinkage, the coating thickness during drying and after drying, the density of the particulate matter, the density of the dry coating and the initial porosity of the coating.

*Calendering model.*—In the calendering process, the rolls of the calender compress the coating in order to reduce the coating thickness and adjust the structure of the porous composite. Meyer et al. investigated the effect of the calendering process on electrode structure.[20] The cause-effect relation between line load $q_{\mathrm{L}}$ and final coating density $\rho_{\mathrm{c}}$ (Eq. 7) and final porosity $\varepsilon_{\mathrm{c}}$ (Eq. 8) was modeled using exponential equations. The equations also require the compaction resistance $\gamma_{\mathrm{c}}$ of the coating in addition to the line load, the initial and maximum density ($\rho_{\mathrm{dry}}$, $\rho_{\mathrm{max}}$) and the initial and minimum porosity ($\varepsilon_{\mathrm{dry}}$, $\varepsilon_{\mathrm{min}}$). The compaction resistance is affected by the used material, formulations, pore structure and roll temperature and can be fitted directly based on measured values using Eqs. 7 or 8. Minimum porosity $\varepsilon_{\mathrm{min}}$ and maximum density $\rho_{\mathrm{max}}$ are determined according to Eqs. 9 and 10 with $\rho_{\mathrm{ph}}$ being the physical density of the solid material.[19,21]

$$\rho_{\mathrm{c}}(q_L) = \rho_{\mathrm{max}} - (\rho_{\mathrm{max}} - \rho_{\mathrm{dry}})\exp\left(-\frac{q_{\mathrm{L}}}{\gamma_{\mathrm{c}}}\right) \quad [7]$$

$$\varepsilon_{\mathrm{c}}(q_{\mathrm{L}}) = \varepsilon_{\mathrm{min}} + (\varepsilon_{\mathrm{dry}} - \varepsilon_{\mathrm{min}})\exp\left(-\frac{q_{\mathrm{L}}}{\gamma_{\mathrm{c}}}\right) \quad [8]$$

$$\varepsilon_{\mathrm{min}} = p \cdot \varepsilon_{\mathrm{dry}} \quad [9]$$

$$\rho_{\mathrm{max}} = (1 - \varepsilon_{\mathrm{min}}) \cdot \rho_{\mathrm{ph}} \quad [10]$$

The coating thickness after calendering $h_{\mathrm{cal}}$ is modeled using a mass balance approach before and after calendering (Eq. 11). The equation requires the coating thickness $h_{\mathrm{dry}}$ and the coating density $\rho_{\mathrm{dry}}$ before calendering and coating density $\rho_{\mathrm{cal}}$ after calendering (provided by Eq. 7).

**Table I. Extract of the governing equations of the P2D standard model. For a complete set of equations see Refs. 27, 28 *L* denotes the full cell thickness and $\delta_{el,a}$ and $\delta_{el,c}$ the layer thickness of anode and cathode, respectively.**

| Equations | | Boundary Conditions | |
|---|---|---|---|
| $\frac{\partial c_s}{\partial t} = \frac{1}{r^2}\frac{\partial}{\partial r}\left(D_s r^2 \frac{\partial c_s}{\partial r}\right)$ | [19] | $\frac{\partial c_s}{\partial r} = \frac{-j^{Li}}{z \cdot F \cdot a_s \cdot D_s}, r = R_p$ | [27] |
| $j^{tot} = \frac{\partial}{\partial x}\left(\sigma_{s,eff}\frac{\partial \phi_s}{\partial x}\right)$ | [20] | $\frac{\partial c_s}{\partial r} = 0, r = 0$ | [28] |
| $\varepsilon\frac{\partial c_e}{\partial t} = \frac{\partial}{\partial x}\left(D_{e,eff}\frac{\partial c_e}{\partial x}\right) + (1 - t_p)\frac{j^{Li}(x)}{F}$ | [21] | $\frac{\partial c_e}{\partial x} = 0, x = \{0, L\}$ | [29] |
| $j^{tot} = -\frac{\partial}{\partial x}\left(\sigma_{e,eff}\frac{\partial \phi_e}{\partial x}\right) - 2\frac{RT}{F}(t_p - 1)\sigma_{e,eff}\frac{\partial \ln c_e}{\partial x}$ | [22] | $\frac{\partial \phi_s}{\partial x} = \frac{-I_{cell}}{A_{cell} \cdot \sigma_{s,eff}}, x = \{0, L\}$ | [30] |
| $j^{tot} = j^{Li} + j^{DL}$ | [23] | $\frac{\partial \phi_s}{\partial x} = 0, x = \{\delta_{el,a}, L - \delta_{el,c}\}$ | [31] |
| $j^{Li} = a_s i_0\left(\exp\left(\alpha\frac{\eta F}{RT}\right) - \exp\left(-(1 - \alpha)\frac{\eta F}{RT}\right)\right)$ | [24] | $\frac{\partial \phi_e}{\partial x} = 0, x = \{0, L\}$ | [32] |
| $i_0 = k_{ct}F(c_e)^{\alpha}(c_{max} - c_s)^{\alpha}(c_s)^{(1-\alpha)}$ | [25] | | |
| $U_{cell} = \phi_s(L) - \phi_s(0)$ | [26] | | |

$$h_{cal} = \frac{\rho_{dry} \cdot h_{dry}}{\rho_{cal}} \quad [11]$$

The approach assumes there is no elongation in lateral and forward direction during calendering. Finally, tortuosity of the calendered electrode $\tau_{cal}$ is acquired using the empirical Bruggeman relation (Eq. 12).[22] The Bruggeman parameter $\beta$ was identified based on the differential effective medium approximation using a top and cross section electrode image by Ebner and Wood.[23]

$$\tau_{cal} = \varepsilon_{cal}^{-\beta} \quad [12]$$

***Battery cell simulation.***—The isothermal electrochemical pseudo-two-dimensional battery model implemented in this research is based on the approach established by Doyle et al.[24] for metal lithium cells and dual lithium insertion cells. The model was further extended by various scientists[25–29] and is approved and applied in a wide range of scientific work.[12,30–33]

The computational model space is discretized in the x-direction from anode to cathode, including the separator. Active material particles in anode and cathode are further discretized in radial coordinates. Fundamental equations and assumptions are discussed briefly in the following. A detailed description can be found in the literature.[24,27,28]

Based on a defined set of structural and material parameters and an applied current the model is able to estimate the cell potential over time. The model takes the main physical processes into account, like reaction kinetics, diffusive and migrative lithium-ion transport and the double layer (dis)charging. It estimates the time dependent state variables, i.e. the solid and liquid phase lithium concentration $c_s$ and $c_e$, the solid and liquid phase potentials $\phi_s$ and $\phi_e$ and the surface overpotentials $\eta$ for both electrodes. From the states of the solid phase potentials, the overall cell potential can be derived (see Eq. 26). The energy density of the cell is calculated by integrating the product of the cell potential and the applied current density over time. The governing model equations are displayed in Table I.

For the model a dual intercalation cell is implemented with the following reaction at both electrodes[28]:

$$Li_s \rightleftharpoons Li_e^+ + V_s + e_s^- \quad [13]$$

with $Li_s$ as the intercalated lithium and $V_s$ as an intercalation vacancy at the surface of the solid particle. The reaction kinetics are described using the Butler-Volmer equation, causing the reaction current $j^{Li}$ (see Eq. 24). The exchange current density $i_0$ thereby is calculated with a concentration dependent reaction rate constant, as previously implemented by Colclasure et al.[28] (see Eq. 25). The active surface area $a_s$ is influenced by the electrode microstructure and is therefore dependent on the manufacturing steps. It can be described as (Eq. 14):

$$a_s = \frac{3 \cdot (1 - \varepsilon)}{R_P} \quad [14]$$

The reaction flux $j^{Li}$ occurring at the surface of the particle provides a boundary condition for the mass transport in the solid particles and the electrolyte, described in Eqs. 19 and 21. Conservation of mass and charge are ensured by Eqs. 19 to 22. The double layer is considered at the particle surface, see Eq. 23. The influence of the electrode microstructure on the transport processes is illustrated by the effective coefficients for diffusion and conductivity. For describing the effective coefficients the Bruggeman relation is established. The effective solid conductivity $\kappa_{s,eff}$ is calculated as:

$$\kappa_{s,eff} = (1 - \varepsilon)\kappa_s^{\beta} \quad [15]$$

The effective electrolyte conductivity $\kappa_{e,eff}$ is described as:

$$\kappa_{e,eff} = \frac{\varepsilon}{\tau}\kappa_e \quad [16]$$

The effective electrolyte diffusion $D_{e,eff}$ is implemented as:

$$D_{e,eff} = \frac{\varepsilon}{\tau}D_e \quad [17]$$

The structural parameters porosity $\varepsilon$ and tortuosity $\tau$ of the electrode are mainly affecting the transport processes and are highly dependent on the manufacturing process. The implemented equations of the correlation between the microstructure and the effective transport coefficients are simplified approximations. Recent publications by Laue et al. and Mistry et al. stated approaches how to improve these approximations.[34–36] The multi-level model approach is able to be extended by these improved models, but this was out of

**Table II. Input parameters for the process chain simulation.**

| | Process parameters | | Structural parameters | |
|---|---|---|---|---|
| Coating | $h_0$ / $\mu$m | 144.90 ± 2.04 | $\rho_{\text{Slurry}}$ / g cm$^{-3}$ | 2.715 |
| | | | $X_{\text{solvent,0}}$ / kg kg$^{-1}$ | 1.00 |
| Drying | $\dot{m}$ / g m$^{-2}$ s$^{-1}$ | 1.00 ± 0.00 | $X_{\text{solvent,EoFS}}$ / kg kg$^{-1}$ | 1.00 |
| | $t$ / s | 200 | $\varepsilon_{\text{dry}}$ / — | 0.47 ± 0.2 |
| Calendering | $q_{\text{L}}$ / N mm$^{-1}$ | 160 ± 11 | $\gamma_{\text{c}}$ / N mm$^{-1}$ | 193.4 ± 4.3 |
| | | | $p$ / — | 0.4 |
| | | | $\rho_{\text{ph}}$ / g cm$^{-3}$ | 4.40 |
| | | | $\alpha$ / — | 0.55 |

the scope of this work for better comparability to other state of the art models.

The presented model homogenizes the electrode structure and neglects local effects. The model provides good results for low and medium discharge rates. With increasing the discharge rate the influence of local effects, which are not represented by the model, increases. Using a 3D microstructure model could resolve this issue. Additionally, the previously presented model extensions for an improved description of the electrode structure can be avoided with a three dimensional battery model.[9,37] In the context of this work, however, a large number of simulation runs were required to perform a stochastic analysis. The used model approach offers a good compromise between accuracy and computational cost.

## Model Parameterization

In this part the presented models are parameterized and validated. The aim of this step is to determine parameters in such a way that measurements can be mapped. For the process models, the process parameters need to be identified so that the structural parameters of the simulation match the structural parameters of the reference electrode. In the case of the battery model the electrochemical measurements were used to estimate kinetic and effective transport parameters for the battery model by identifying the simulation on the measurements with a least square algorithm approach.

***Process chain simulation.—***The process chain simulation uses parameters from Jaiser et al.[16] and Meyer et al.[20,21] for the coating, drying and calendering processes. The simulation was applied to produce cathodes with a mean coating thickness $h_{\text{cal}}$ of around 65 $\mu$m and a porosity $\epsilon_{\text{cal}}$ of 0.31. Based on the process models and the parameters of the three processes, an initial wet coating thickness $h_0$ of 144.90 $\mu$m was determined. Table II shows the process and structural parameters for the individual process steps. The standard deviations for the process parameters are based on data of the machines used in the work by Meyer et al. The deviations of the drying rate $\dot{m}$ and the drying time $t$ do not affect the structural parameters since they are employed to predict the final film thickness only (see Eq. 4). Thus, no standard deviations were considered for the drying rate and the drying time. The structural parameters were kept constant except for the porosity of the dried electrode $\varepsilon_{\text{dry}}$ and the compaction resistance $\gamma_{\text{c}}$. The standard deviation for both parameters were set according to measurements in the Battery LabFactory Braunschweig.

***Battery model.—***Electrochemical experiments were conducted with a three-electrode setup. Therefor PAT-Cells from the EL-CELL GmbH were used. They use a cylindrical electrode with a diameter of 18 mm and a separator with an included lithium reference electrode. Graphite and NMC622 were used for the anode and cathode and were produced by the ZSW in Ulm, Germany. For each electrode the OCP curves were measured. The structural data of the electrodes are displayed in Table III. The electrolyte was 1.0 M $LiPF_6$ in EC:EMC (3:7 in weight) with 2 wt% VC. The separator is a glass fiber separator by EL-CELL GmbH (ECC1-00-0210-O/X). All experiments were conducted in an ESPEC SU-642 temperature chamber at (25 ± 0.3) °C. The assembled PAT-Cells were used to measure the electrochemical properties. The MACCOR 4000 test system was used to perform the formation of the cells and a discharge rate capability test. For the formation step, the cells were charged and discharged three times with a constant current step at 0.1 C in the voltage range of 2.9 V to 4.2 V. The discharge rate

**Table III. Battery model parameters used in the applied model. The diffusion coefficient in the electrolyte, ionic conductivity and transference number are dependent on electrolyte concentration.**

| Parameter | Symbol | Unit | Anode | Separator | Cathode |
|---|---|---|---|---|---|
| Layer thickness[a)] | $\delta$ | m | $63.5 \times 10^{-6}$ | $100 \times 10^{-6}$ | $65.1 \times 10^{-6}$ |
| Porosity[a)] | $\varepsilon$ | — | 0.399 | 0.5 | 0.313 25 |
| Particle size[a)] | $R_P$ | m | $9.50 \times 10^{-6}$ | — | $5.00 \times 10^{-6}$ |
| Tortuosity[b)] | $\tau$ | — | 2.09 | 1.0 | 1.896 |
| Maximum capacity solid[b)] | $c_{\text{Max}}$ | mol m$^{-3}$ | 32 741 | — | 44 949 |
| Initial capacity solid[b)] | $c_0$ | mol m$^{-3}$ | 32 132 | — | 17 827 |
| Initial capacity electrolyte[b)] | $c_e$ | mol m$^{-3}$ | 1200 | 1200 | 1200 |
| Diffusion coefficient solid[b)] | $D_s$ | m$^2$ s$^{-1}$ | $3.75 \times 10^{-12}$ | — | $2.96 \times 10^{-15}$ |
| Diffusion coefficient electrolyte[d)] | $D_e$ | m$^2$ s$^{-1}$ | $f(c)$[38] | $f(c)$[38] | $f(c)$[38] |
| Electronic conductivity[b)] | $\kappa_s$ | S m$^{-1}$ | 0.0116 | — | 6.8215 |
| Ionic conductivity[d)] | $\kappa_e$ | S m$^{-1}$ | $f(c)$[38] | $f(c)$[38] | $f(c)$[38] |
| Transference number[d)] | $t_p$ | — | $f(c)$[38] | $f(c)$[38] | $f(c)$[38] |
| Charge transfer coefficient[c)] | $\alpha$ | — | 0.5 | — | 0.5 |
| Reaction rate constant[b)] | k | — | $1.36 \times 10^{-8}$ | — | $2.72 \times 10^{-11}$ |
| Double layer capacity[c)] | $C_{\text{DL}}$ | F m$^{-2}$ | 0.2 | — | 0.2 |

a) measured by ZSW (department of production research). b) adjusted. c) set, from Ref. 27. d) concentration dependence, see Eq. in Ref. 38.

capability test was performed at three different discharge rates of 0.5 C, 1 C and 2 C in a voltage range from 2.9 V to 4.2 V.

In the first step of the parametrization, the OCP curves for the electrode materials are identified with the following Redlich-Kister approach[28]:

$$E_{\text{ref}}^{\text{eq}} = \frac{\Delta G_{33}^{\circ}}{F} + \frac{RT}{F}\ln\left(\frac{1 - X_{\text{Li}^{\text{I}}}}{X_{\text{Li}^{\text{I}}}}\right) + \frac{1}{F}\sum_{m=0}^{N} A_{\text{m}}\left[(2X_{\text{Li}^{\text{I}}} - 1)^{m+1} - \left(\frac{2mX_{\text{Li}^{\text{I}}}(1 - X_{\text{Li}^{\text{I}}})}{(2X_{\text{Li}^{\text{I}}} - 1)^{1-m}}\right)\right] \quad [18]$$

A least square algorithm is used to identify the Redlich-Kister coefficients $A_m$ for the anode and cathode. The estimated coefficients are listed in Table VIII (see Appendix). The final set of parameters for the battery model is listed in Table III. The adjusted parameters were defined with a least square based parametrization step. The kinetic model parameters were adjusted to represent the measurements with the simulation. The determined parameters were compared with the literature and are of a similar order of magnitude.[14,28,35] The electrical conductivity of the anode is below the usual values, however, in literature comparable results due to different causes in manufacturing and sample preparation are estimated.[12] The parameterized model is able to reproduce the electrochemical performance of the assembled lithium-ion batteries for the investigated discharge rates (see Fig. 11, Appendix). Minor discrepancies between the simulation and the measurements may result from the homogenization of the electrode structure. This effect increases with an increasing discharge rate. Overall, the parameterized model is considered sufficiently accurate to map the measurements.

The parameterization and validation only apply to the reference point. Small scale deviations around the reference point can be represented, but with a reduced precision. This allows to realize the scope of the work, i.e. to study the general propagation and impact of minor uncertainties around a reference value for lithium ion battery electrode production.

## Case Study

This section describes the case study applied to the model approach in this work. It was chosen in such a way that the effect of manufacturing tolerances, i.e. varying process parameters, on the structural parameters and the electrochemical properties of a lithium-ion battery can be studied. The case study is thus used to reveal the propagation and interactions of uncertain structural parameters along the consecutive process steps and study the influence of varying structural parameters on electrochemical properties. The models presented in the methodology section are validated for the parameterized reference cell. The estimated uncertainties for the structural parameters and the electrochemical properties are not validated, but will be compared to literature.

For the case study, the previously presented process chain simulation with process models for the coating, drying and calendering processes is considered. Uncertainties are only taken into account for the manufacturing of the cathode, the anode parameters are kept constant. Four distinct manufacturing scenarios, illustrated in Fig. 2, are discussed where each has a different combination of uncertainties along the manufacturing chain. The first scenario is defined as the nominal scenario, as all processes are assumed to be free of process and parameter uncertainties in order to provide a reference scenario. In the other scenarios, the porosity after the drying process always varies because the formation of the electrode structure in the drying process is subject to natural variation caused by the non-uniform evaporation of the solvent. A constant value of the porosity cannot be achieved even with very tight tolerances. In addition, uncertainties occur in at least one other manufacturing step. Scenario two assumes uncertain parameters due to the coating and drying processes. The applied mass loading varies, as an uncertain coating thickness is applied on the substrate in the coating process, also the slurry density is an uncertain structural input parameter resulting for example from deviations in the previous mixing and dispersing process. Scenario three considers variations caused by the drying and calendering process. Here, the minimal porosity $\varepsilon_{\text{c,min}}$, the maximal density $\rho_{\text{c,max}}$, the resistance factor $\gamma_{\text{c}}$ and the line load $q_{\text{L}}$ are assumed to be uncertain. The line load is the varying process parameter for this manufacturing step. The other parameters vary due to uncertainties in the material. Finally, scenario four assumes that uncertainties arise from all three manufacturing processes. Mean values and standard deviations for the input process and structural parameters for each manufacturing step are displayed in Table IV.

For each scenario the manufacturing process of 500 cells were simulated in the process chain simulation. The varying input parameters for each cell were estimated with a Monte-Carlo based approach. For each input parameter a Gaussian distribution was assumed. For this study only cell-to-cell variations are considered, i.e. each parameter is assumed to be constant within a single cell, but parameters vary between cells. Variations over the thickness and the area of the electrode are not considered. In the work of Laue et al. these aspects were considered and analyzed.[8] The assumed uncertainties in the manufacturing process lead to uncertainties in the structural parameters entering the battery model. These are: the

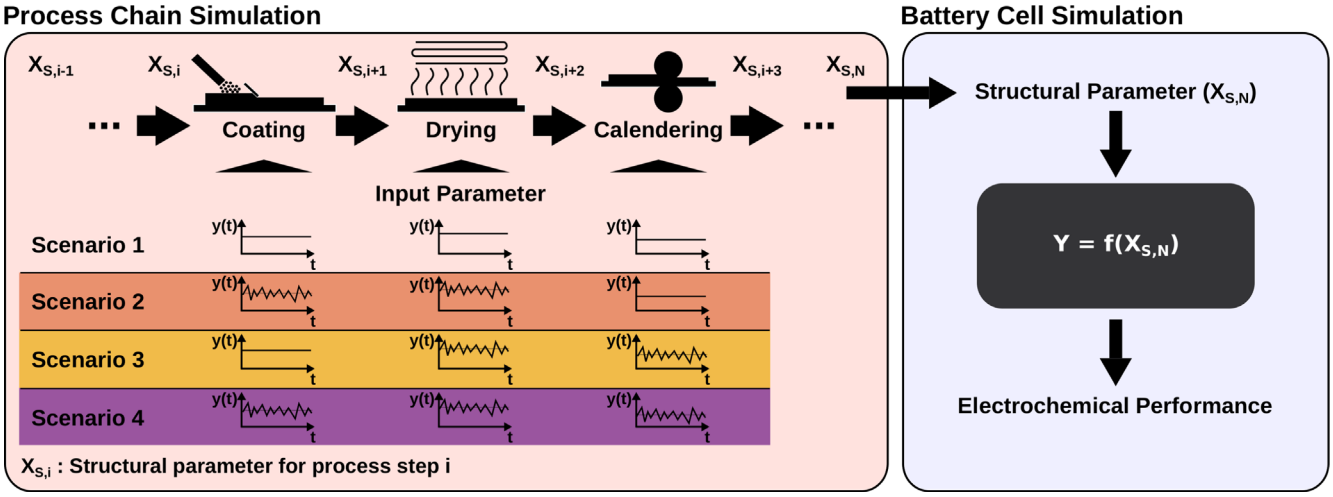


**Figure 2.** Displayed is the basic model approach and the scenarios that were simulated for the case study.

**Table IV. Uncertain input parameters for the process models in the process chain simulation for scenarios S1–S4. Mean values are given in scenario one, and deviations in scenario two to four.**

| | Coating | | Drying | Calendering | | | |
|---|---|---|---|---|---|---|---|
| Parameter<br>Unit | $M_{wet}$<br>mg cm$^{-2}$ | $\rho_{slurry}$<br>g cm$^{-3}$ | $\varepsilon_{dry}$<br>— | $\varepsilon_{min}$<br>— | $\rho_{max}$<br>g cm$^{-3}$ | $\gamma_c$<br>N mm$^{-1}$ | $q_L$<br>N mm$^{-1}$ |
| S1 | 39.3 | 2.72 | 0.470 | 0.232 | 3.38 | 592 | 642 |
| S2 | ±0.4 | ±0.03 | ±0.009 | — | — | — | — |
| S3 | — | — | ±0.009 | ±0.002 | ±0.03 | ±12 | ±44 |
| S4 | ±0.4 | ±0.03 | ±0.009 | ±0.002 | ±0.03 | ±12 | ±44 |

**Table V. Mean value, standard deviation and relative standard deviation of the resulting structural parameters after calendering for the cathode thickness, porosity and tortuosity with the implemented process models. These structural parameters are used as input parameters for the battery cell simulation.**

| Parameter<br>Unit | Layer thickness $\delta_C$<br>$\mu$m | Porosity $\varepsilon_C$<br>— | Totuosity $\tau_C$<br>— |
|---|---|---|---|
| S1 | 65.09 | 0.3124 | 1.896 |
| S2 | 65.05 ± 1.95(±3%) | 0.3122 ± 0.003(±1.06%) | 1.897 ± 0.011(±0.58%) |
| S3 | 65.12 ± 0.76(±1.17%) | 0.3124 ± 0.007(±2.29%) | 1.897 ± 0.024(±1.25%) |
| S4 | 65.12 ± 2.16(±3.31%) | 0.3131 ± 0.007(±2.28%) | 1.894 ± 0.024(±1.25%) |

thickness, porosity and tortuosity of the cathode. The volumetric energy density is chosen as the main performance property for evaluating the effect of uncertainties in the manufacturing on the cell performance, because it contains the effect of a varying discharge capacity and the voltage losses, and thus is capable of evaluating the performance. The energy density depends on the modus of operation. All simulations are conducted at four different discharge rates: 0.1 C, 0.3 C, 0.5 C and 1 C. Understanding the impact of uncertainties for different C-Rates will also allow to identify and thus to tailor the manufacturing process for maximum allowable deviations for a given battery application.

## Results and Discussion

The results part is divided in two parts. In the first section the correlation between the manufacturing processes and the electrode structure generated from the process chain simulation is discussed. In the second part, the influence of the uncertain structural parameters on the electrochemical properties of the cells is evaluated, and the findings are connected to the insights of the first part. This leads to a continuous analysis of the interactions and uncertainties from the process to the structure to the electrochemical properties.

***Manufacturing impact on structural parameters.—***In this part the impact of uncertainties in the manufacturing processes on the electrode structure will be analyzed. The uncertainties were estimated based on the process models presented in the methodology section and the input parameters listed in Table IV. In Table V, the resulting mean values, standard deviations and relative standard deviations for cathode thickness, porosity and tortuosity are listed for each scenario after the calendering process. Based on the data in the table, it can be seen that the mean value of the structural parameters remain relatively constant for all manufacturing scenarios. The layer thickness of the cathode shows high deviations for scenario two and four. The standard deviation of the porosity and tortuosity of the cathode is high for scenario three and four.

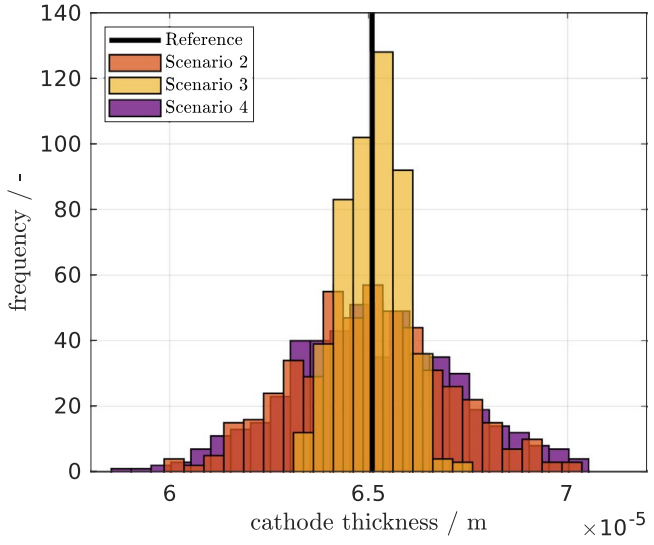


**Figure 3.** Histograms of the cathode thickness for the different scenarios.

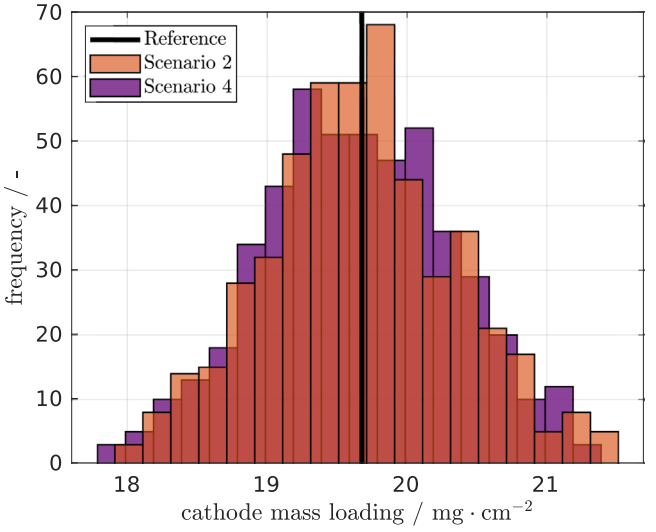


**Figure 4.** Histograms of the mass loading for the different scenarios. The mass loading is constant for scenario 3, due to the constant coating process.

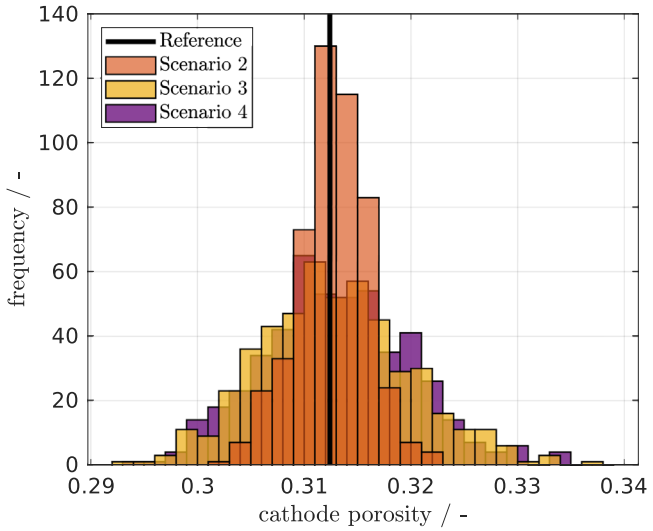


**Figure 5.** Histograms of the cathode porosity for the different scenarios.

In the following paragraphs the determined uncertainties for the layer thickness, porosity and tortuosity are discussed in relation to the manufacturing scenarios and compared to literature values.

In Fig. 3, the distributions of the cathode thickness for the different manufacturing scenarios are displayed. The width of the distribution is greatest for scenario two and four and narrowest for scenario three. The second scenario deals with the influence of uncertainties in the coating and drying process, while the fourth scenario is a combination of the second and third scenario (see Table IV). The results show that the cathode layer thickness is mainly affected by uncertainties in the coating process. Due to Eq. 1, the variation of the layer thickness is based on the uncertain mass loading applied on the substrate. According to the scenarios, the mass loading varies for scenario two and four, but stays constant for scenario three (Fig. 4). The distribution of the cathode layer thickness estimated for scenario four can be compared to the results of scenario two. This is supported by the values of the standard deviation and relative standard deviation in Table V. It can be concluded that the cathode layer thickness and the mass loading are sensitive to uncertainties in the coating process. Furthermore, the calendering process is effective at setting a certain electrode thickness even if the calendering process itself is not that accurate, but it cannot maintain or adjust a constant height if a varying mass loading is applied, due to uncertainties in the coating process.

In Fig. 5, the distributions of the cathode porosity for the simulated scenarios are displayed. In contrast to Fig. 3, the width of the distribution is greatest for scenario three and four and narrow for scenario two. In the third scenario, uncertainties arise in the drying and calendering process, while the fourth scenario is a combination of the second and third scenario. Taking the figure and the values for the standard deviation and the relative standard deviation into consideration it can be concluded that the cathode porosity is sensitive against uncertainties in the calendering process. Furthermore, it can be observed that for a constant calendering process (scenario 2) the relative standard deviation of the porosity is lowered from approximately 2% after the drying process (see Table IV) to 1.06% after the calendering process. The constant calendering step led to a homogenization of the porosity within the cathode. This is caused by the process control of the calendering process. Applying a constant line load leads to an evenly adjusted porosity of the electrode after calendering, as thicker electrode sections are compressed with the same force. The effect of the line load on the porosity is discussed in depth by Meyer et al.[21] This is also the reason why a constant line load in the calendering process does not lead to a homogenization of the layer thickness. The use of a gap-controlled machine would lead to an interaction between the layer thickness and the porosity, since thicker sections of the electrode are also more strongly calendered.

The distribution of the cathode tortuosity is displayed in Fig. 6. The resulting distributions are comparable to the results of the cathode porosity due to the calculation of the tortuosity based on Eq. 12 with a constant Bruggemann coefficient.

In a study from Hoffmann et al.,[39] the deviation of structural parameters for pilot production processes were analyzed. For a double-sided coating process the deviations of the layer thickness for the cathode was approximately ±0.89 $\mu$m. This is slightly above the estimated values for the process chain simulation. In the study a double-sided coating process was analyzed and the complexity of the applied models in the process chain simulation are limited. However, the structural parameters generated with the model are comparable to the results of the work. For the porosity of the cathode, Hoffmann evaluated a deviation of ±1.73% and this can be compared to the results of the process chain simulation. The tortuosity of the electrodes were not evaluated in the work of Hoffmann.

In summary, it can be stated that the manufacturing steps considered in this study have a varying impact on the structural parameters and the effect could be estimated with the model approach. Within the framework of the process models used in this study, the following assumptions arise:

- **Scenario 1:** Reference—no uncertainties in all manufacturing steps.
- **Scenario 2:** Load dominated—high uncertainties for the mass loading and the cathode thickness due to the uncertainties in the coating process.
- **Scenario 3:** Porosity dominated—high uncertainties for the porosity due to uncertainties in the calendering process.
- **Scenario 4:** Combination—high uncertainties for the thickness, porosity and tortuosity due to uncertainties in all manufacturing steps.

Furthermore, it can be concluded that for the applied models in this study no relevant interactions and superposition between the thickness and the porosity occur, due to the process control of the calendering step. Changing the process models and the process control will result in a different outcome.

***Battery performance.***—In this part, the propagation of the uncertainties in structural parameters and the impact on the electrochemical performance properties is analyzed. In combination with the results from the previous section, conclusions can be made on how uncertainties in the manufacturing process affect the

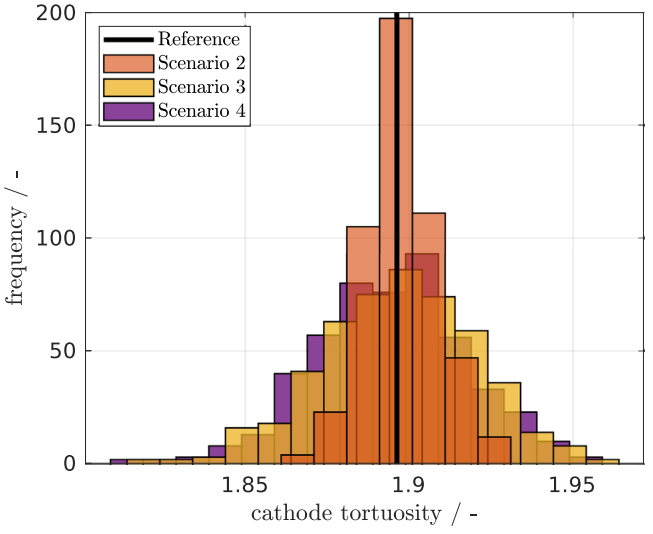


**Figure 6.** Histograms of the cathode tortuosity for the different scenarios.

performance of the simulated battery. The estimated varying structural parameters (see Table V) are taken as an input for the battery model. Also included are the measured, identified and chosen parameters listed in Table III.

Firstly, the distribution of the volumetric energy density is studied in depth as an indicator for the electrochemical performance properties. Simulations were conducted at 0.1 C, 0.3 C, 0.5 C and 1 C. The results for 0.5 C are not discussed in detail, as they follow the trend of the other discharge rates. In Fig. 7, the distributions for the different manufacturing scenarios are plotted for all considered discharge rates. The mean value, standard deviation and relative standard deviation extracted from these data are listed in Table VI. Based on these results it can be stated that the mean value of the volumetric energy density remains approximately constant for a certain discharge rate for all scenarios. Additionally the results show, that an increasing discharge rate leads to a decreasing energy density. The load dominated and the combined scenario (Scenario 2 and 4) show always the widest distribution. The shape of the resulting distribution for the energy density is skewed for low discharge rates and the shape and the width shifts to a Gaussian distribution with increasing discharge rate.

In order to gain a deeper understanding of how uncertainties of structural parameters affect the electrochemical performance properties, three essential aspects of the electrochemical simulations will be analyzed in the following. Firstly, limiting processes of the reference scenario are analyzed. This is used to explain the sensitivity of the uncertainties on the electrochemical performance properties. In the second part, the effect of uncertainties in varying manufacturing steps on the volumetric energy density is studied in depth and sensitive parameters and processes are identified. The last part deals with how the different shapes of distributions arise and how they can be interpreted and evaluated.

*Analysis of the physical limitations of the reference battery.*—The decrease of the energy density with increasing discharge rates results from slow solid diffusion in the cathode active material particles. The analysis of the results for the reference case shows that for all discharge rates the lithium concentration in the active material particles of the cathode is not uniform (Fig. 8). Whereas it is uniform for the anode with a maximum lithium concentration difference of 0.5% at high discharge rates between the inner particle and the area close to the surface. The depletion in the cathode particles happens due to the relatively slow solid diffusion compared to the fast reaction kinetics at the surface of the particle for higher discharge rates. Further the lithium-ion transport in the electrolyte is not limiting the performance of the battery for the considered discharge rates up to 1 C as the lithium ion concentration in the electrolyte does not drop under 1000 mol $m^{-3}$. In Fig. 8 the lithium concentration in the cathodic solid particles at a discharge rate of 0.1 C is close to the maximum lithium concentration of 44949 mol $m^{-3}$ (see Table III) at the surface, thus the utilization of the active material at the cathode is relatively high. The lithium concentration of the anode in the solid particles is relatively low with around 800 mol $m^{-3}$ at 0.1 C. This indicates, that the battery is well balanced at a discharge rate of 0.1 C. Increasing the cathode layer thickness leads to a limitation of the discharge capacity due to an undersized anode, while decreasing the cathode thickness leads to a limiting cathode. This aspect is discussed in depth in the following parts.

*Impact of the uncertainties in varying manufacturing processes on the volumetric energy density.*—Uncertainties in the the mass loading based on tolerances in the coating process have a significant effect on the distribution of volumetric energy density. From nominal behavior the simulation results show that for all discharge

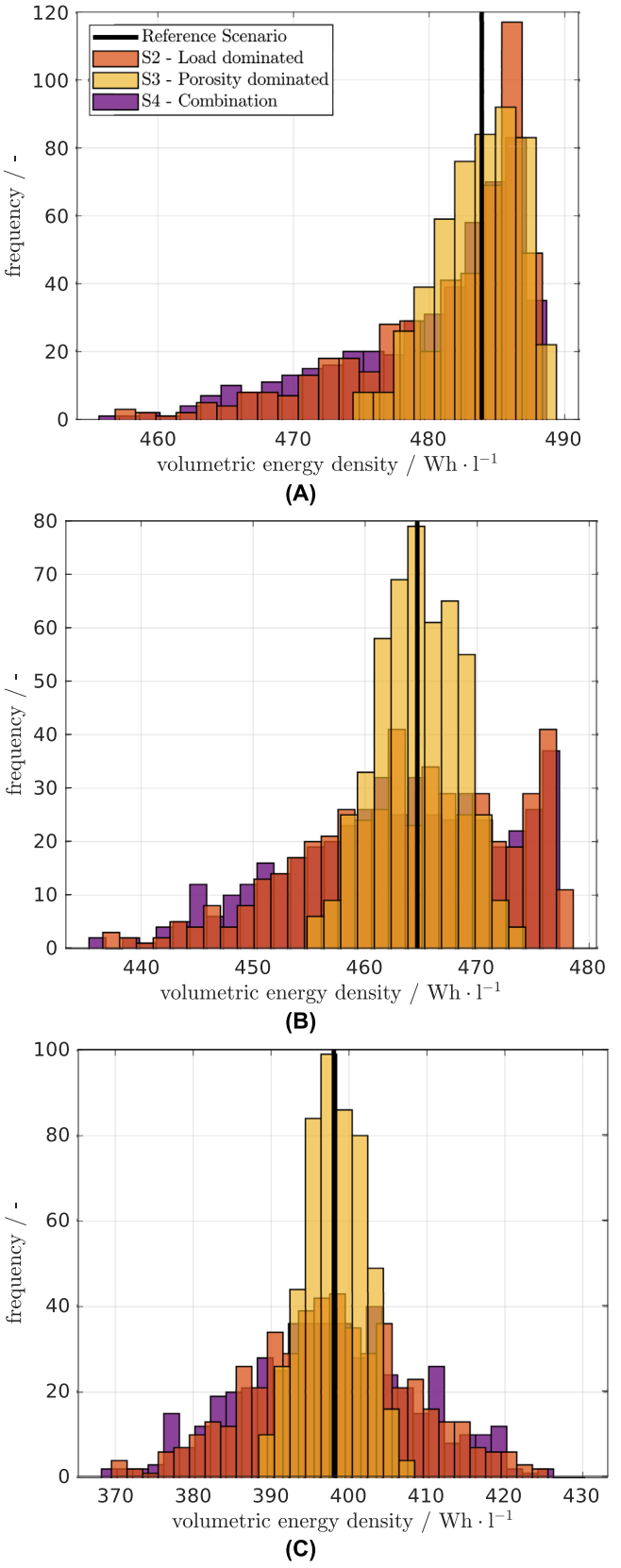


**Figure 7.** Histograms of the volumetric energy density estimated with the battery model. Included are the different scenarios and three different discharge rates 0.1 C (a), 0.3 C (b), 1 C (c).

**Table VI. Mean value, standard deviation and relative standard deviation for the estimated energy density for each discharge rate.**

| Property<br>Unit | Energy Density at 0.1 C<br>W h $l^{-1}$ | Energy Density at 0.3 C<br>W h $l^{-1}$ | Energy Density at 1 C<br>W h $l^{-1}$ |
|---|---|---|---|
| S1 | 483.88 | 464.66 | 398.06 |
| S2 | 480.97 ± 6.43(±1.34%) | 463.81 ± 9.05(±1.95%) | 397.91 ± 10.48(±2.63%) |
| S3 | 483.64 ± 3.08(±0.64%) | 464.78 ± 3.72(±0.80%) | 398.21 ± 3.75(±0.94%) |
| S4 | 480.38 ± 6.84(±1.42%) | 463.34 ± 9.57(±2.07%) | 397.54 ± 11.07(±2.78%) |

**Table VII. Mean value, standard deviation and relative standard deviation for the estimated discharge capacity for each discharge rate.**

| Property<br>Unit | Capacity at 0.1 C<br>A h $m^{-2}$ | Capacity at 0.3 C<br>A h $m^{-2}$ | Capacity at 1 C<br>A h $m^{-2}$ |
|---|---|---|---|
| S1 | 30.09 | 29.11 | 25.66 |
| S2 | 29.88 ± 0.65(±2.2%) | 29.06 ± 0.84(±2.9%) | 25.65 ± 0.91(±3.6%) |
| S3 | 30.07 ± 0.24(±0.8%) | 29.11 ± 0.28(±0.97%) | 25.67 ± 0.28(±1.1%) |
| S4 | 29.85 ± 0.69(±2.3%) | 29.04 ± 0.89(±3.1%) | 25.63 ± 0.96(±3.8%) |

rates the deviation of the energy density is greatest for scenario two (load dominated) and four (combination). Uncertainties in the mass loading lead to similar relative standard deviations for the discharge capacities of the individual cells as for the volumetric energy density (Table VII). This behavior is also described by An et al.,[4] who showed that the deviation of the discharge capacity is correlated to the variation of the cell weight. The third manufacturing scenario (porosity dominated) is characterized by uncertain porosity and tortuosity. These variations mainly affect the kinetics of the electrode. The effective transport coefficients are varying due to both uncertain structural parameters. The effective ionic conductivity and the effective diffusion coefficient in the electrolyte vary around ±2.19%, and the effective solid conductivity varies around ±0.64%. Additionally the active surface area is changing due to the uncertainties in the porosity of the cathode. The active surface area varies at around ±0.64%. Overall the deviations of the effective transport coefficient have a minor effect on the electrochemical performance, due to the non-existent limitation in the transport processes in the electrolyte discussed previously.

In Fig. 9, the energy densities for every simulated cell for all scenarios are plotted for different discharge rates. Additionally, a surface plot illustrates the dependence of the volumetric energy density on changing thickness and porosity of the cathode. The surface is generated by deterministic simulation using an equidistant variation of cathode thickness and porosity. Note that although tortuosity variation is not taken into account the results of the scenarios are located on the surface. This shows the low impact of tortuosity for this surface generation, on the volumetric energy density (max. deviation approx. 0.005%).

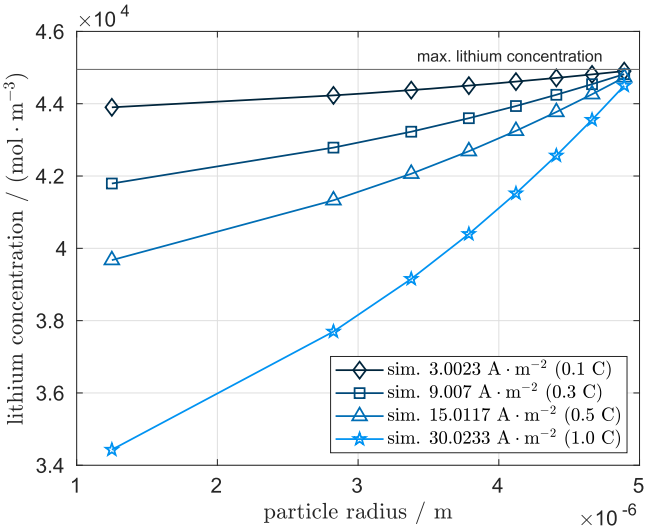


**Figure 8.** Lithium concentration in the solid particles of the cathode averaged over the electrode thickness for the reference scenario at the end of discharge.

Based on the figure it can also be concluded that the manufacturing scenarios lead to differently arranged distributions on the surface. If the variation induced by the process is oriented in the direction of a steep slope, the process has a significant impact on the volumetric energy density. The load dominated scenario (S2) and the combined scenario (S4) are defined by their wide distribution of the cathode thickness, thus they are oriented toward a steep gradient of the surface. The porosity dominated scenario (S3) is oriented in the direction of a flat gradient of the surface. Hence, S2 has more impact on the battery performance than S3. The combined model approach thus is able to identify the coating process as the most sensitive one. The results indicate to first tackle the tolerances in the coating process, due to the high sensitivity on the volumetric energy density.

*Shape and width of the distributions for varying discharge rates.*—The analysis of the distributions for the volumetric energy density shows that for low discharge rates of 0.1 C and 0.3 C, skewed distributions and not Gaussian distributions are obtained for the volumetric energy density (see Fig. 7). At higher discharge rates of 1 C, the shape of the distribution shifts in the direction of a Gaussian distribution. To evaluate quantitatively whether the estimated distributions are normally distributed, a one-sample Kolmogorov-Smirnov test was conducted. The test statistic is the maximum absolute difference between an empirical cumulative distribution function describing the data and a hypothesized cumulative distribution function. The hypothesis is either accepted or rejected. The one-sample Kolmogorov-Smirnov test leads to the conclusion that the distributions are not Gaussian distributed with a 5% significance level for all discharge rates.

The shape and the width of the distribution is mainly affected by the behavior of the volumetric energy density in the considered uncertainty range of the structural parameters. In Fig. 9, the surface plot visualizes the behavior of the volumetric energy density as a function of layer thickness and porosity for a low discharge rate. Characteristic for the surface plot is the ridge defining an optimal volumetric energy density depending on the cathode layer thickness and the cathode porosity. This is decisively influenced by the utilization of the electrodes as discussed in the part of the physical limitations of the reference battery in this section . Additionally, it is observed that the slope in front of the ridge, i.e. for low cathode thicknesses, is steeper than behind it. Two different processes can be

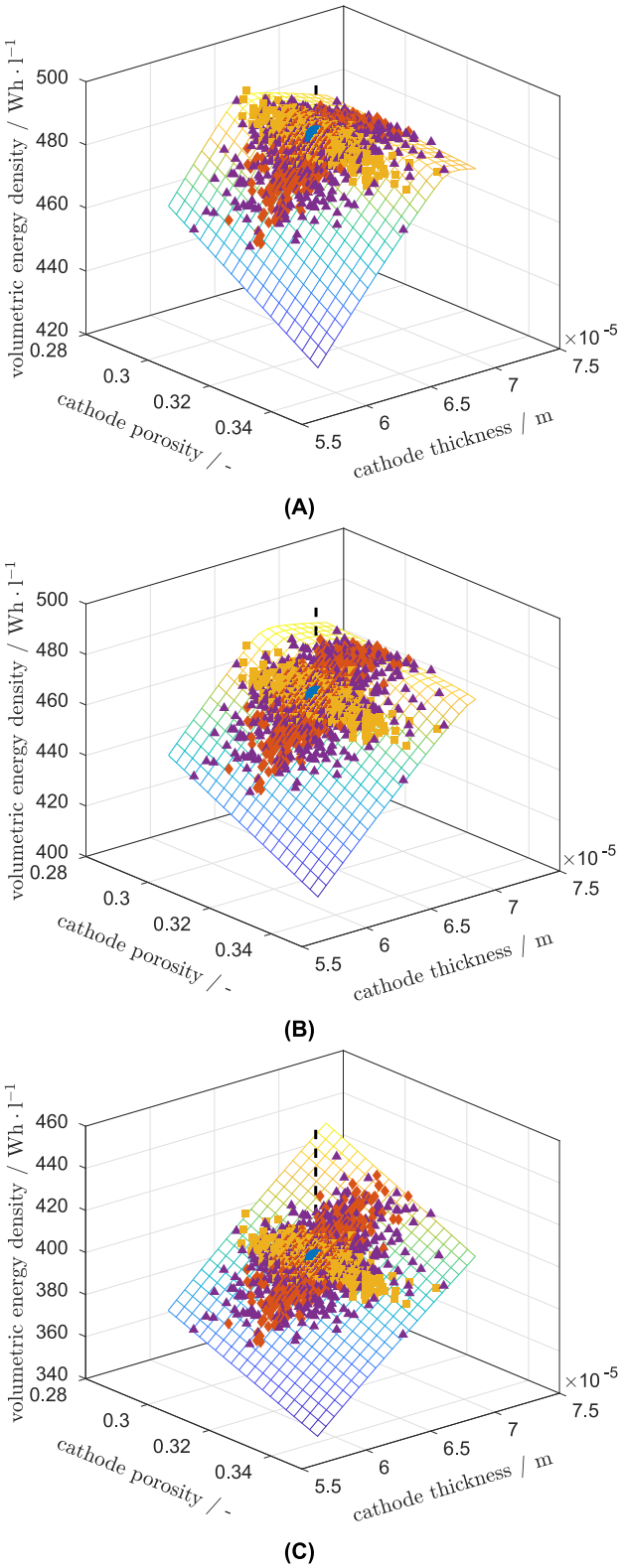


**Figure 9.** Simulated energy densities for three different discharge rates 0.1 C (a), 0.3 C (b), 1 C (c). Grid: model results for equidistant variation in porosity and thickness, symbols are results of the reference case (•) and scenarios (△). The colours are consistent to the previous plots. Blue: Scenario 1, Red: Scenario 2, Yellow: Scenario 3, Purple: Scenario 4.

related to this behavior. For low cathode layer thicknesses the volumetric energy density is increasing with thickness, because the mass loading in the cathode is increased and thus the storage capacity for lithium in the active material is enhanced. Hence, the cathode is limiting the performance. Behind the ridge, i.e. for thick cathodes, the volumetric energy density is decreasing, because increasing the cathode mass loading leads to a not fully utilized capacity of the cathode, and unused active material is added and the anode is the limiting electrode. Thus the volumetric energy density decreases.

Increasing the mass loading is also achieved by reducing the porosity of the cathode. This leads to an orientation of the ridge non-orthogonal to the varying layer thickness. Furthermore, the surface is slightly tilted. This happens due to the consideration of the volumetric energy density. At lower cathode layer thickness and porosity, the discharge capacity and the overpotentials are almost identical, but the volume of the battery is smaller due to the reduced layer thickness. The impact of the lower porosity could be seen by looking at the gravimetric energy density. In summary, it can be seen that there is a non-linear dependence of the volumetric energy density on the layer thickness and the porosity.

The location and orientation of the uncertainties on the previously described surface is crucial for whether a skewed distribution occurs. This aspect will be illustrated at an simplified example shown in Fig. 10.

The distribution function $h_1(x)$ represents a deviation of the input $x$, e.g. the thickness, and is chosen as a Gaussian distribution. The distribution function $h_1(x)$ is transferred to the distribution function $h_2(y)$, which represents the distribution of the output, e.g. the energy density. Distributions are transferred using simple function $f(x)$, e.g. describing the battery performance. We show two examples for the function $f(x)$. A second order polynomial function with a maximum within the distribution of $h_1(x)$ is shown in Fig. 10a. It can be seen that functions with non linearity yields skewing of the function $h_2(y)$ and the functions maximum yields an upper bound for the output distribution $h_2(y)$. In contrast a linear function only yields transfer of the variables proportional to the slope, but preserves the distribution shape. With this in mind the results in Figs. 7 and 9 will be discussed in more detail.

In Fig. 9a, the volumetric energy density for 0.1 C is plotted. It is observed, that the volumetric energy density of the reference battery is located on the ridge of the meshed surface and the variations cluster around this reference point. The orientation of the deviations arising in Scenario 2 and 4 is mainly arranged in the direction of the cathode thickness and nearly orthogonal to the ridge. This orientation and location lead to the skewed shape of the distribution, analogous to the behavior described in Fig. 10a. Increasing the discharge rate up to 0.3 C, the reference battery and the variations are located further away from the ridge of the meshed area (see Fig. 9b). This happens due to the effect of the kinetic limitations in the solid diffusion in the cathode particles illustrated and discussed in the part of the physical limitations and in Fig. 8. The optimum shifts in the direction of thicker cathodes, because the increased volume leads to a decrease of the reaction current $j^{\mathrm{Li}}$, and the thicker cathode has the ability to store more lithium despite the limitation of solid diffusion and thus leads to a higher utilization of lithium in the anode. The impact of the optimum is still visible in the histogram of 0.3 C in Fig. 9b which reveals that a bimodal shape of the distribution exists for this discharge rate. Increasing the discharge rate up to 1 C, the impact of the kinetics on the volumetric energy density increases and the simulated cells move further away from the ridge and are located in an area of an approximately constant slope (see Fig. 9c). A Gaussian distribution in an area of a constant slope will lead to a Gaussian distribution. This behavior is analogous to the linear function illustrated in Fig. 10b. This effect is observed in Fig. 7: with increasing the discharge rate, the shape of the distributions is close to a Gaussian distribution.

Additionally, it can be observed that the width of the distribution is increasing while increasing the discharge rate. In Table VI it can be seen, that the standard deviation for the volumetric energy density is increasing more rapidly for scenario two and four. This effect also results from the less skewed shape of the distributions at higher

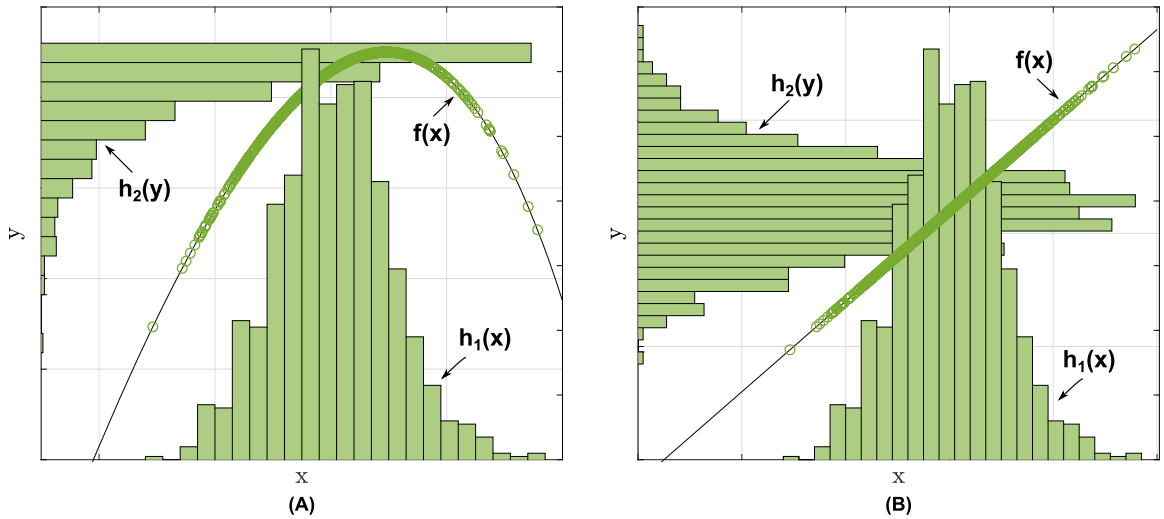


**Figure 10.** Illustration of the impact of an uncertain input parameter x with Gaussian distribution on the output y. This is shown for an arbitrary function with an optimum (a) and an arbitrary linear function (b).

discharge rates and the increased slope. While the shape is shifting, the distributions start to spread out, due to the more normalized shape and a steep constant slope.

The values estimated for the capacity displayed in Table VII can be compared to the results generated by Hoffmann et al.[39] The overall capacity for Hoffmann is at around 39.60 Ah $m^{-2}$. This is slightly higher than for the cells studied in this study. The standard deviation for Hoffmann is given at around 1.14 Ah $m^{-2}$. This is also above the values estimated in this study, but overall the range of the deviation can be compared between these two studies. Taking into account the simplifications done in this study, e.g. not considering the whole manufacturing chain and the reduced precision of the battery model in terms of the microstructure, a reasonable prediction of the electrochemical performance and the varying performance is achieved.

## Conclusion and Outlook

This work contributes to understand the propagation of uncertainties arising in the manufacturing process of lithium-ion battery electrodes and to quantify the effect of these on the electrochemical performance properties. Therefor, a model approach is implemented which on the one hand describes the manufacturing process of electrodes with the help of process models and on the other hand analyzes the product by means of a physical-based battery cell simulation. The coupling of the two model parts via the transferred structural parameters leads to a coherent consideration of the various parameter levels and allows to study the propagation of uncertainties starting from the origin in the manufacturing process until the lithium-ion battery performance. This is in contrast to literature which usually studies process-structure interactions either experimentally or analyzes structure-performance relationships with models. Thus, this work bridges the parameters for processes, structure and performance. It establishes a platform that is able to estimate the impact of uncertainties for the first time and is capable to perform mathematical optimizations in a reasonable time frame. The implemented model was parameterized on a reference cell, and a case study was conducted with four cases. The scenarios differed in the origin of the uncertainties in the manufacturing process and were based on plausible deviations. The performance of the reference cell is limited by the solid diffusion in the active material particles of the cathode. The evaluation of the case study showed that the model approach is able to identify that among the investigated processes, the coating process has the highest impact on the deviations in the volumetric energy density. Tight tolerances are required for the coating thickness and thus the mass loading of the electrode due to the high impact on the volumetric energy density. Additionally, it was observed that deviations close to an optimum leads to skewed distributions. Analyzing the data of manufacturing cells and observing a skewed distribution could thus be an indicator for manufacturing a battery close to the performance optimum.

The coupled simulation platform is able to estimate the impact of tolerances in the manufacturing processes on the electrochemical performance properties and identify the sensitive process parameters. The chosen models and the associated assumptions create additional model uncertainties which must be taken into account when considering the results. Additionally, the correlations presented here only apply to the particular cell considered in the case study. Choosing a different cell may lead to different results due to changed parameters.

In this study, the approach of joint battery production and performance modeling was implemented for the first time and the propagation and effect of process uncertainties on performance could be studied in depth. In the future, the process models may to be refined and adapted for a better description of the electrode structure and better correlation to the process parameters. The implementation of the process chain model is modular and can be understood as a platform that can be easily extended. Due to the low computational costs, mathematical methods like sensitivity analysis and robust optimization can be applied for knowledge-driven optimization of the electrode manufacturing process. This will additionally lead to cost reductions due to lower discard and specific optimization of the most important contributors to battery performance variation.

## Acknowledgments

This work was supported by the German Federal Ministry of Education and Research (BMBF) through funding the project "Multi-Level-Simulation of Product-Process-Interdependencies (Sim2Pro)" (grant number 03XP0075). Further the authors gratefully thank our project partners "QS-Zell" (grant number 03XP0076A) from ZSW (Department of Production Research) and "HighEnergy" (grant number 03XP0073C) from ZSW for providing the electrodes and the related data.

## Appendix

In Section 3.2 the measurements and the parametrization of the battery model is described. In Table VIII the estimated Redlich-Kister coefficients for graphite (anode) and NMC622 (cathode) are

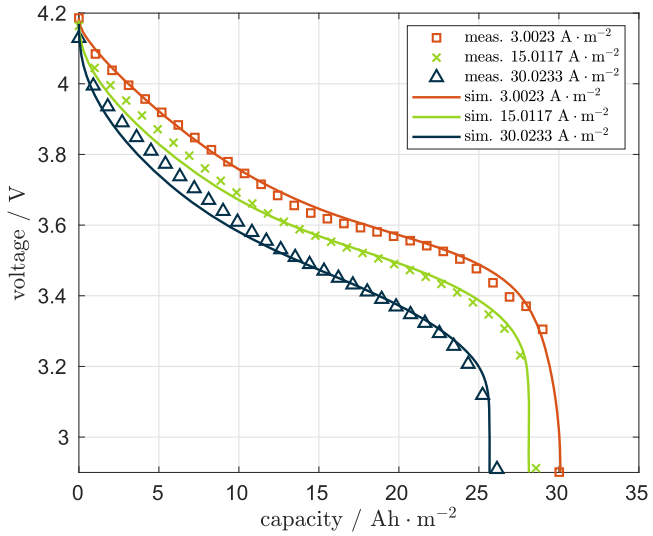


**Figure 11.** Comparison of the discharge rate measurements and simulations.

**Table VIII. Estimated Redlich-Kister coefficients for the anode and cathode.**

| Coefficient | Value Anode | Value Cathode |
|---|---|---|
| $\mu^0_{\mathrm{Li^I}}$ | −13623.95 | −400702.35 |
| $A_0$ | −3573.16 | −68925.68 |
| $A_1$ | 5627.51 | 23 521.86 |
| $A_2$ | −4017.09 | 11 647.96 |
| $A_3$ | 4545.96 | −5984.28 |
| $A_4$ | −4118.16 | −7485.09 |
| $A_5$ | 4140.82 | 5098.95 |
| $A_6$ | −4145.24 | — |
| $A_7$ | 4046.99 | — |
| $A_8$ | −4152.91 | — |
| $A_9$ | 4033.88 | — |
| $A_{10}$ | −4166.47 | — |
| $A_{11}$ | 4070.92 | — |
| $A_{12}$ | −4166.68 | — |
| $A_{13}$ | 4062.00 | — |
| $A_{14}$ | −4150.00 | — |
| $A_{15}$ | 4102.28 | — |
| $A_{16}$ | −4166.73 | — |

listed for the parametrization of the open cell potential (OCP) curve. These are input parameters for the battery model.

In Fig. 11 the measured discharge curves for three different current densities are plotted with the dotted lines. The results of the parametrized battery model for these current densities are plotted with the solid lines. A good agreement between the measured and simulated curves can be observed.

List of Symbols

| | | |
|---|---|---|
| Latin letters | | |
| $A_{cell}$ | cell area | $m^2$ |
| $a_s$ | active surface area | $m^{-1}$ |
| $c_e$ | concentration electrolyte | mol $m^{-3}$ |
| $c_{max}$ | maximum concentraion | mol $m^{-3}$ |
| $c_s$ | concentration solid | mol $m^{-3}$ |
| $D_e$ | diffusion coefficient electrolyte | $m^2$ $s^{-1}$ |
| $D_{e,eff}$ | effective diffusion coefficient electrolyte | $m^2$ $s^{-1}$ |
| $D_s$ | diffusion coefficient solid | $m^2$ $s^{-1}$ |
| F | farraday constant | C $mol^{-1}$ |
| $G°_{33}$ | standard state chemical potantial of an intercalated lithium | kg $m^2$ $s^{-2}$ |
| $h_0$ | initial wet coating thickness | m |
| h(t) | coating thickness during drying | m |
| $h_{dry}$ | coating thickness after drying | m |
| $h_{cal}$ | coating thickness after calendering | m |
| $i_0$ | exchange current density | A $m^{-2}$ |
| $I_{cell}$ | cell current | A |
| $j^{DL}$ | double layer current density | A $m^{-3}$ |
| $j^{LI}$ | reaction flux | A $m^{-3}$ |
| $j^{tot}$ | total current density | A $m^{-3}$ |
| $k_{ct}$ | reaction rate constant | $s^{-1}$ |
| $\dot{m}$ | drying rate | kg $s^{-1}$ |
| $M_{solid}$ | mass loading of solid | kg $m^{-2}$ |
| $M_{solvent}$ | mass loading of solvent | kg $m^{-2}$ |
| $M_{wet}$ | mass loading of wet film | kg $m^{-2}$ |
| $q_L$ | line load | N $mm^{-1}$ |
| R | ideal gas constant | J $mol^{-1}$ $K^{-1}$ |
| $R_P$ | particle size | m |
| T | temperature | K |
| t | drying time | s |
| $t_p$ | transference number | — |
| $t_{EoFS}$ | time until end of film shrinkage | s |
| $U_{cell}$ | cell voltage | V |
| $X_{Li}{}^{I}$ | intercalation fraction | — |
| $X_{solvent,0}$ | liquid-to-solid ratio of the coating | — |
| $X_{solvent,EoFS}$ | liquid-to-solid ratio at the end of film shrinkage | — |
| z | number of electrons | — |
| Greek letters | | |
| $\alpha$ | charge transfer coefficient | — |
| $\beta$ | Bruggeman parameter | — |
| $\gamma_c$ | compaction resistance | $m^{-1}$ |
| $\varepsilon$ | porosity | — |
| $\varepsilon_c$ | final porosity after calendering | — |
| $\varepsilon_{dry}$ | initial porosity of the coating | — |
| $\varepsilon_{min}$ | minimum porosity | — |
| $\eta$ | overpotential | V |
| $\kappa_e$ | ionic conductivity | S $m^{-1}$ |
| $\kappa_{e,eff}$ | effective ionic conductivity | S $m^{-1}$ |
| $\kappa_s$ | solid conductivity | S $m^{-1}$ |
| $\kappa_{s,eff}$ | effective solid conductivity | S $m^{-1}$ |
| $\rho_c$ | final density after calendering | kg $m^{-3}$ |
| $\rho_{dry}$ | density of the dry coating | kg $m^{-3}$ |
| $\rho_{max}$ | maximum density | kg $m^{-3}$ |
| $\rho_{ph}$ | physical density | kg $m^{-3}$ |
| $\rho_{PM}$ | density of the particulate matter | kg $m^{-3}$ |
| $\rho_{slurry}$ | density of the slurry | kg $m^{-3}$ |
| $\tau$ | tortuosity | — |
| $\tau_{cal}$ | tortuosity of calendered electrode | — |
| $\phi_e$ | potential electrolyte | V |
| $\phi_s$ | potential solid | V |

## ORCID

Ulrike Krewer https://orcid.org/0000-0002-5984-5935

## References

1. A. Kwade, W. Haselrieder, R. Leithoff, A. Modlinger, F. Dietrich, and K. Droeder, "Current status and challenges for automotive battery production technologies." *Nat. Energy*, **3**, 290 (2018).
2. D. Shin, M. Poncino, E. Macii, and N. Chang, "A statistical model of cell-to-cell variation in Li-ion batteries for system-level design." *Proceedings of the International Symposium on Low Power Electronics and Design*, 94 (2013).
3. G. Berckmans, M. Messagie, J. Smekens, N. Omar, L. Vanhaverbeke, and J. V. Mierlo, "Cost projection of state of the art lithium-ion batteries for electric vehicles up to 2030." *Energies*, **10**, 1314 (2017).
4. F. An, L. Chen, J. Huang, J. Zhang, and P. Li, "Rate dependence of cell-to-cell variations of lithium-ion cells." *Sci. Rep.*, **6**, 35051 (2016).

5. S. Santhanagopalan and R. E. White, "Quantifying cell-to-cell variations in lithium ion batteries." *International Journal of Electrochemistry*, **2012**, 395838 (2012).
6. N. Lin, X. Xie, R. Schenkendorf, and U. Krewer, "Efficient global sensitivity analysis of 3d multiphysics model for Li-ion batteries." *J. Electrochem. Soc.*, **165**, A1169 (2018).
7. M. Hadigol, K. Maute, and A. Doostan, "On uncertainty quantification of lithium-ion batteries: application to an $LiC_6/LiCoO_2$ cell." *Journal of Power Sources*, **300**, 507 (2015).
8. V. Laue, O. Schmidt, H. Dreger, X. Xie, F. Röder, R. Schenkendorf, A. Kwade, and U. Krewer, "Model-based uncertainty quantification for the product properties of lithium-ion batteries." *Energy Technology*, **8**, 1900201 (2019).
9. A. C. Ngandjong, A. Rucci, M. Maiza, G. Shukla, J. Vazquez-Arenas, and A. A. Franco, "Multiscale simulation platform linking lithium ion battery electrode fabrication process with performance at the cell level." *The Journal of Physical Chemistry Letters*, **8**, 5966 (2017).
10. M. Chouchane, A. Rucci, T. Lombardo, A. C. Ngandjong, and A. A. Franco, "Lithium ion battery electrodes predicted from manufacturing simulations: assessing the impact of the carbon-binder spatial location on the electrochemical performance." *Journal of Power Sources*, **444**, 227285 (2019).
11. A. Rucci, A. C. Ngandjong, E. N. Primo, M. Maiza, and A. A. Franco, "Tracking variabilities in the simulation of lithium ion battery electrode fabrication and its impact on electrochemical performance." *Electrochimica Acta*, **312**, 168 (2018).
12. G. Lenze, F. Röder, H. Bockholt, W. Haselrieder, A. Kwade, and U. Krewer, "Simulation-supported analysis of calendering impacts on the performance of lithium-ion-batteries." *J. Electrochem. Soc.*, **164**, A1223 (2017).
13. J. Smekens, R. Gopalakrishnan, N. Van den Steen, N. Omar, O. Hegazy, A. Hubin, and J. Van Mierlo, "Influence of electrode density on the performance of Li-ion batteries: experimental and simulation results." *Energies*, **9**, 104 (2016).
14. B. Kenney, K. Darcovich, D. D. MacNeil, and I. J. Davidson, "Modelling the impact of variations in electrode manufacturing on lithium-ion battery modules." *Journal of Power Sources*, **213**, 391 (2012).
15. J. K. Mayer, L. Almar, E. Asylbekov, W. Haselrieder, A. Kwade, A. Weber, and H. Nirschl, "Influence of the carbon black dispersing process on the microstructure and performance of Li-ion battery cathodes." *Energy Technology*, **8**, 1900161 (2019).
16. S. Jaiser, J. Kumberg, J. Klaver, J. L. Urai, W. Schabel, J. Schmatz, and P. Scharfer, "Microstructure formation of lithium-ion battery electrodes during drying–an ex situ study using cryogenic broad ion beam slope-cutting and scanning electron microscopy (Cryo-BIB-SEM)." *Journal of Power Sources*, **345**, 97 (2017).
17. M. Schönemann, *Multiscale Simulation Approach for Battery Production Systems* (Springer International Publishing) (2017).
18. M. Thomitzek, O. Schmidt, F. Röder, U. Krewer, C. Herrmann, and S. Thiede, "Simulating process-product interdependencies in battery production systems." *Procedia CIRP*, **72**, 346 (2018).
19. C. Meyer, M. Weyhe, W. Haselrieder, and A. Kwade, "Heated calendering of cathodes for lithium-ion batteries with varied carbon black and binder contents." *Energy Technology*, **8**, 1900175 (2019).
20. C. Meyer, H. Bockholt, W. Haselrieder, and A. Kwade, "Characterization of the calendering process for compaction of electrodes for lithium-ion batteries." *Journal of Materials Processing Tech.*, **249**, 172 (2017).
21. C. Meyer, M. Kosfeld, W. Haselrieder, and A. Kwade, "Process modeling of the electrode calendering of lithium-ion batteries regarding variation of cathode active materials and mass loadings." *Journal of Energy Storage*, **18**, 371 (2018).
22. D. A. G. Bruggeman, "Berechnung verschiedener physikalischer Konstanten von heterogenen Substanzen. III. die elastischen konstanten der quasiisotropen mischkörper aus isotropen substanzen." *Ann. Phys. (Berlin)*, **421**, 160 (1937).
23. M. Ebner and V. Wood, "Tool for tortuosity estimation in lithium ion battery porous electrodes." *J. Electrochem. Soc.*, **162**, A3064 (2015).
24. M. Doyle, T. F. Fuller, and J. Newman, "Modeling of galvanostatic charge and discharge of the lithium/polymer/insertion cell." *J. Electrochem. Soc.*, **140**, 1526 (1993).
25. T. F. Fuller, M. Doyle, and J. Newman, "Simulation and optimization of the dual lithium ion insertion cell." *J. Electrochem. Soc.*, **141**, 1 (1994).
26. J. Newman, K. E. Thomas, H. Hafezi, and D. R. Wheeler, "Modeling of lithium-ion batteries." *Journal of Power Sources*, **119-121**, 838 (2003).
27. N. Legrand, S. Raël, B. Knosp, M. Hinaje, P. Desprez, and F. Lapicque, "Including double-layer capacitance in lithium-ion battery mathematical models." *Journal of Power Sources*, **251**, 370 (2014).
28. A. M. Colclasure and R. J. Kee, "Thermodynamically consistent modeling of elementary electrochemistry in lithium-ion batteries." *Electrochimica Acta*, **55**, 8960 (2010).
29. K. Smith and C. Y. Wang, "Solid-state diffusion limitations on pulse operation of a lithium ion cell for hybrid electric vehicles." *Journal of Power Sources*, **161**, 628 (2006).
30. R. Darling and J. Newman, "Modeling a porous intercalation electrode with two characteristic particle sizes." *J. Electrochem. Soc.*, **144**, 4201 (1997).
31. F. Röder, S. Sonntag, D. Schröder, and U. Krewer, "Simulating the impact of particle size distribution on the performance of graphite electrodes in lithium-ion batteries." *Energy Technology*, **4**, 1588 (2016).
32. G. Sikha, B. N. Popov, and R. E. White, "Effect of porosity on the capacity fade of a lithium-ion battery." *J. Electrochem. Soc.*, **151**, A1104 (2004).
33. V. Ramadesigan, R. N. Methekar, F. Latinwo, R. D. Braatz, and V. R. Subramanian, "Optimal porosity distribution for minimized ohmic drop across a porous electrode." *J. Electrochem. Soc.*, **157**, A1328 (2010).
34. V. Laue, N. Wolff, F. Röder, and U. Krewer, "Modeling the influence of mixing strategies on micro structural properties of all solid state electrodes." *Energy Technology*, **8**, 1801049 (2019).
35. V. Laue, F. Röder, and U. Krewer, "Joint structural and electrochemical modeling: impact of porosity on lithium-ion battery performance." *Electrochimica Acta*, **314**, 20 (2019).
36. A. N. Mistry, K. Smith, and P. P. Mukherjee, "Secondary-phase stochastics in lithium-ion battery electrodes." *ACS Appl. Mater. Interfaces*, **10**, 6317 (2018).
37. T. Danner, M. Singh, S. Hein, J. Kaiser, H. Hahn, and A. Latz, "Thick electrodes for Li-ion batteries: a model based analysis." *Journal of Power Sources*, **334**, 191 (2016).
38. L. S. Kremer, A. Hoffmann, T. Danner, S. Hein, B. Prifling, D. Westhoff, C. Dreer, A. Latz, V. Schmidt, and M. Wohlfahrt-Mehrens, "Manufacturing process for improved ultra-thick cathodes in high-energy lithium-ion batteries." *Energy Technology*, **8**, 1900167 (2019).
39. L. Hoffmann, J. K. Grathwol, W. Haselrieder, R. Leithoff, T. Jansen, K. Dilger, K. Dröder, A. Kwade, and M. Kurrat, "Capacity distribution of large lithium-ion battery pouch cells in context with pilot production processes." *Energy Technology*, **8**, 1900196 (2019).